Heterogeneous Nucleation Promotes Carrier Transport in Solution-Processed Organic Field-Effect Transistors

*Ruipeng Li, Hadayat Ullah Khan, Marcia M. Payne, Detlef-M. Smilgies, John E. Anthony, and Aram Amassian**

A new way to investigate and control the growth of solution-cast thin films is presented. The combination of in situ quartz crystal microbalance measurements with dissipation capabilities (QCM-D) and in situ grazing-incidence wide-angle X-ray scattering (GIWAXS) in an environmental chamber provides unique quantitative insights into the time-evolution of the concentration of the solution, the onset of nucleation, and the mode of growth of the organic semiconductor under varied drying conditions. It is demonstrated that careful control over the kinetics of solution drying enhances carrier transport significantly by promoting phase transformation predominantly via heterogeneous nucleation and sustained surface growth of a highly lamellar structure at the solid-liquid interface at the expense of homogeneous nucleation.

1. Introduction

In organic electronics, the development of high-performance and soluble small-molecule semiconductors has enabled field-effect mobilities of better than ≈1 $cm^2 V^{-1} s^{-1}$ in solution-cast thin films,[1–7] with recent reports of mobilities in solution-processed organic field-effect transistors (OFETs) even surpassing 10 $cm^2 V^{-1} s^{-1}$.[8] This high performance requires the microstructure and morphology of solution-cast thin films, which develops via nucleation and growth processes, to exhibit a high degree of crystallinity with two-dimensional in-plane π-stacking, a high purity of lamellar texturing, a low density of grain/domain boundaries, low crystallographic misorientation at boundaries, and high surface coverage of the substrate.[9–12] Efforts to tune the microstructures and morphologies of solution-cast thin films have been hampered by the lack of understanding and control over the nucleation and growth of the thin films as the solution undergoes phase transformation. Instead, much of the recent success stems almost exclusively from ex situ characterization combined with trial-and-error methods, with a few recent exceptions.[6,11,13]

Vacuum processing of organic semiconductors, on the other hand, has developed into a mature and widely accepted thin film deposition method for electronics and other applications because of the availability of in situ thin film diagnostic techniques, ranging from simple microbalance rate monitors to more sophisticated electron-based scattering, spectroscopy and microscopy,[2,14,15] to X-ray-based scattering and absorption,[16–18] to scanning probe microscopy.[19] Time-resolved investigation of solution drying to reveal the intricacies of the phase transformation process is hampered by the inaccessibility of the solution environment to most vacuum-based characterization probes, while rapid drying makes the use of in situ scanning probe microscopy and neutron scattering techniques inappropriate for most common experimental conditions.[20,21]

Here, we quantify and control the nucleation and growth of solution-cast thin films of 6,13-bis(triisopropylsilylethynyl) pentacene (TIPS-Pn), a highly soluble small-molecule semiconductor which can be solution-cast to yield OFETs with mobilities of up to 4.6 $cm^2 V^{-1} s^{-1}$.[6,10] Combining in situ quartz crystal microbalance measurements with dissipation capabilities (QCM-D) with in situ grazing-incidence wide-angle X-ray scattering (GIWAXS) in an environmental chamber, we provide unique and unprecedented qualitative and quantitative insights into the nucleation and growth of organic semiconductors prepared under varied conditions of solution drying. By controlling the kinetics of solution drying, the onset of heterogeneous nucleation, the rate of thin film growth, R_d, and, importantly, the relative dominance of surface incorporation versus bulk nucleation, we tune the microstructure and morphology of thin films, and consequently modulate the field effect mobility in OFETs by nearly two orders of magnitude.

2. Results and discussion

The concentration of the drying solution, $C(t)$, is known to determine the nucleation behavior for a given solution and

Dr. R. Li, Dr. H. U. Khan, Prof. A. Amassian
Materials Science and Engineering Program
Division of Physical Science and Engineering
King Abdullah University of Science and Technology
Thuwal 23955-6900, Saudi Arabia
E-mail: Aram.Amassian@kaust.edu.sa
Dr. D.-M. Smilgies
Cornell High Energy Synchrotron Source
Cornell University
Ithaca, NY 14850, USA
Dr. M. M. Payne, Prof. J. E. Anthony
Department of Chemistry
University of Kentucky
Lexington, KY 40506, USA

DOI: 10.1002/adfm.201201264

substrate;[22] determining $C(t)$ is therefore of paramount importance to relating the nucleation and growth behaviors, and ultimately the thin film microstructure, to the solution casting conditions. Measuring the mass of the drying solution with respect to casting time, t, is an easy and reliable method to estimate the mean concentration up to the onset of nucleation, $t = t^*$. This yields a linear dependence with respect to time (see **Figure 1**a), as expected in conditions of constant evaporation rate, E, and $C \propto t^{-1}$. Hence, prior to nucleation ($t \leq t_c$), $C(t)$ can be estimated as

$$C(t) = \frac{Y_{max}}{V} = \frac{Y_{max}}{V_0 - \frac{ES}{\rho}t} \quad (1)$$

where Y_{max} is the total amount of solute, V_0 and V are the starting and current volumes, respectively, ρ is the solution density and S is the effective casting surface area on the substrate. This greatly simplifies the estimation of the critical concentration (C^*) of the solution on condition that nucleation can also be detected. In doing so, it is important to distinguish between nucleation and crystallization.

In situ GIWAXS (Figure 1a,b) and QCM-D measurements (Figure 1c,d) are used to detect the onsets of crystallization and mass deposition, as well as the kinetics of crystallization and thin film growth, respectively. In situ GIWAXS measurements were performed under identical conditions of solution-casting using an environmental chamber, as shown in Figure 1a, to detect the onset of crystallization, the kinetics of crystal growth, as well as the packing structure and texture of the films.[23] GIWAXS measurements of the as-cast dry film (cf. Figure S1a, Supporting Information) reveal a highly lamellar ordered film, shown by the series of (00l) peaks (l = 1, 2, 3) with $q_z = 3.81$ nm^{-1} and an equivalent interplanar d-spacing of 1.65 ± 0.02 nm for the (001) Bragg sheet.[8] The two isotropic rings at q = 2.6 and 5.5 nm^{-1} originate from the two Kapton windows of the chamber. The inset of Figure S1a (Supporting Information) shows a GIWAXS image taken at t = 289 s, just seconds prior to the onset of nucleation. The broad isotropic ring originates from the solvent with no evidence of long-range order. Onset of crystallization of the lamellar structure is shown in Figure 1a, revealing that the crystalline phase is nucleated at t^* = 295 s for C^* = 1.6 wt%. However, as we will reveal below, C^* is overestimated in conditions of ambient and fast drying, due to the resulting buildup of solute near the liquid-air interface. The local critical concentration required for nucleation at the solid-liquid interface is shown below to be closer to ≈1 wt%.

QCM-D senses changes in frequency (ΔF) and energy dissipation (ΔD) associated with the total mass deposited on or bound to the quartz sensor and its viscoelastic properties or rigidity.[24,25] The mass deposited and the liquid-to-solid phase transformation of the solute at the solid-liquid interface can therefore be monitored unambiguously during the drop-casting process under different processing conditions, while changes in the unbound mass located in the bulk and at the surface of the solution can be conveniently ignored. QCM-D also exhibits significant loss of sensitivity to adsorbed mass away from its radial center, making it conveniently insensitive to edge effects, including coffee ring formation.[26] In Figure 1c,d, we show the baseline values of ΔF (≈–310 Hz) and ΔD (≈120 × 10^{-6}), respectively, associated with the pure solvent (dashed red lines) after drop-casting 200 µL of solvent on the microbalance at t = 0. The finite ΔF and ΔD

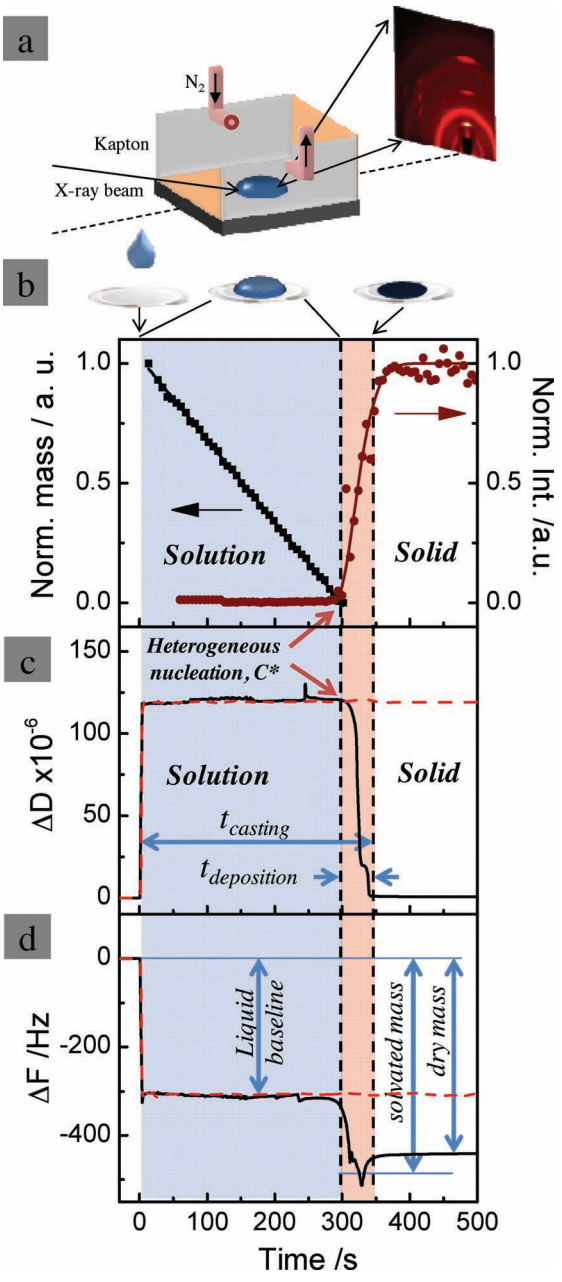

Figure 1. In situ measurements performed during drop-casting of a TIPS-Pn solution in a controlled environment, monitored by a,b), GIWAXS and balance and c,d) by QCM-D. a) The illustration of the closed vapor chamber allowing to control the drying speed and to perform in situ GIWAXS simultaneously. b) The normalized change in mass and intensity of the (001) Bragg sheet of TIPS-Pn during a typical drop-casting experiment in ambient conditions. The solid line following the experimental GIWAXS data points corresponds to an Avrami model fit of the crystallization process. c) The dissipation shift (ΔD) and d) the frequency shift (ΔF) of the pure solvent drop (dashed red lines) and of the drying TIPS-Pn solution (solid black line) in relation to the process time. The process time is initiated (t = 0) upon casting the solution. The key kinetic parameters of drop-casting, including the total casting time ($t_{casting}$), the deposition time ($t_{deposition}$), the solvated mass (minimum ΔF) and the dry mass (steady state of ΔF), are defined in (a) and (b) and allow us to estimate the deposition rate (see text for details). All solutions and casting experiments are prepared/performed at room temperature.

values are related to the viscosity, shear modulus, and density of the solvent liquid and are determined by the characteristic length of the evanescent shear wave of the quartz crystal localized in the liquid medium near the solid-liquid interface. The baseline values therefore remain stable even as the solvent evaporates from the surface of the solution, allowing high sensitivity in the detection of submonolayer changes in bound or deposited masses of solute at the solid-liquid interface near the center of the sensor. The drop-casting experiment of a 4 μL solution of TIPS-Pn (solid black lines) left to dry under ambient conditions on a quartz sensor is also shown in Figure 1b,c. The ΔF and ΔD undergo a step increase at $t > 0$ and are hardly distinguishable from the pure solvent until $\Delta D \rightarrow 0$ at $t > 295$ s, indicating no significant deposition at the solid-liquid interface in the presence of the bulk solution. The coincidence of mass deposition (as sensed by QCM-D) and crystallization (as detected by GIWAXS) proves that growth is initiated by heterogeneous nucleation of lamellar crystallites. The end of the phase transformation process responsible for thin film deposition is detected as $\Delta D = 0$, making it possible to delineate the duration of thin film deposition, $t_{deposition}$, from the onset of decrease of ΔD from its bulk liquid value until $\Delta D = 0$ and the total casting time, $t_{casting}$, from the onset of drop-casting until $\Delta D = 0$. We find these to be $t_{deposition} = 45 \pm 0.1$ s and $t_{casting} = 340$ s in ambient drying conditions ($E \approx 2.2 \times 10^{-5}$ μg mm^{-2} s^{-1}) as per QCM-D. In situ GIWAXS measurements suggest that crystallization continues for a few seconds longer, which can be attributed to evaporation of the residual solvent trapped in the film, in agreement with ΔF measurements shown in Figure 1d. The frequency shift in Figure 1c stabilizes for $t > 350$ s at a value of $\Delta F = -440$ Hz, corresponding to a dry film thickness of ≈55.3 ± 0.2 nm, as per the Sauerbrey equation.[27] With unambiguous determination of the deposition time by QCM-D, we calculate the mean deposition rate, R_d, to be $R_d = 1.23 \pm 0.01$ nm s^{-1} in ambient drying conditions. To gauge run-to-run reproducibility, we have performed 10 attempts in ambient drying conditions. We find a mean deposition time of $t_d = 45.0 \pm 3.2$ s and a final thickness of 52.9 ± 7.1 nm, yielding a deposition rate of $R_d = 1.23 \pm 0.09$ nm s^{-1}. For these same runs, the critical concentration is found to be $C^* = 1.57 \pm 0.13$ wt%, consistent with the in situ GIWAXS finding.

In an effort to tune the nucleation behavior, we varied the drying conditions of the solution by enclosing the sample in an environmental chamber to slow down or speed up the evaporation process by controlling the flow rate of N_2 gas under otherwise identical conditions of solution preparation and casting. In **Figure 2**a, we plot C^* with respect to E and R_d, ranging from 3 × 10^{-6} to 7 × 10^{-5} μg cm^{-2} s^{-1} and from 0.1 to 4 nm s^{-1}, respectively. Two regimes are clearly distinguishable: a rate-invariant regime with $C^* \approx 1$ wt% when E and R_d are substantially slower than ambient conditions, and a rate-dependent regime where C^* scales with $\sim R_d^{0.73}$ and rises continuously as high as ≈4 wt% for $R_d \approx 4$ nm s^{-1}. This is a surprising outcome a priori, because drying proceeds via evaporation from the top surface of the solution, far from the solid-liquid interface. It is believed, however, that rapid evaporation leads to accumulation of the solute near the liquid-air interface, thus allowing a concentration gradient to be established. The limited diffusivity of the solute therefore leaves the local concentration at the solid-liquid interface significantly lower than the concentration of the overall solution, which is determined from measurements of total mass. At reduced rates of evaporation of toluene at room temperature, the solute can achieve uniform distribution throughout the solution via diffusion, insuring the local concentration at the solid-liquid interface to be equal to the bulk concentration. We therefore conclude that heterogeneous nucleation on SiO_2 occurs when $C^* \approx 1$ wt% locally near the solid-liquid interface.

The next important step is to calculate $C(t)$ for $C > C^*$ so that we may know when $C(t)$ reaches the solubility limit, C_B, upon which homogeneous nucleation becomes possible. $C(t)$ can be estimated by accounting for the depletion of solute from the solution upon heterogeneous nucleation and growth of the crystalline thin film, as described by the Avrami model,[28,29] such that:

$$C(t) = \frac{Y_{max} - Y_s}{V} = \frac{Y_{max} e^{K(t-t^*)\eta}}{V_0 - \frac{ES}{\rho}t} \quad (2)$$

Here, Y_s is the instantaneous amount of crystalline material, K is the apparent crystallization rate constant and n is the Avrami exponent related to the dimensionality of the crystallization process. K and n are determined from a model fit to the time-evolution of $I_{(001)}$ (see Figure 1b for the fit and Figure S1b (Supporting Information) for Avrami parameters under differing drying conditions).[30] The resulting $C(t)$ is plotted as a function of normalized casting time ($t/t_{casting}$) in Figure 2b for the experiment performed in ambient environment, as well as two additional deposition experiments monitored by QCM-D and in situ GIWAXS and performed at $R_d = 0.26$ and 2.28 nm s^{-1}. For comparison, $C(t)$ is plotted as a function of casting time in Figure S2 (Supporting Information) for the same three experiments. The temporal coincidence of the onsets of nucleation (by QCM-D) and crystallization (by GIWAXS) revealed in Figure S1b (Supporting Information) for all three rates of drying demonstrates that pre-crystallization at the edge of the drop plays a minor role in the conditions investigated.

The functional form of $C(t)$ in Figure 2b is strikingly dependent upon the speed of drying. At ambient and higher speeds of evaporation, $C(t)$ resembles a t^{-1} functional form, suggesting that the nucleation and growth processes are dominated by the drying behavior of the solution. By contrast, the slower rate of drying leads to a significant deviation from t^{-1}, with $C(t)$ dipping well below C^* as nucleation and growth of the TIPS-Pn lamellae depletes the solution of its solute at a faster pace than the concentration is allowed to rise by evaporation of the solvent. Key differences are also seen in the onset of homogeneous nucleation. Conditions of ambient and faster drying are conducive to rapid onset of homogeneous nucleation, whereas slower deposition leads to $C < C_B$ throughout the drying process, favoring heterogeneous nucleation and surface-dominated growth.

The fraction of solute that transforms to solid via surface growth, i.e., for $C < C_B$, is presented in Figure 2c. In ambient conditions of drying, only ≈40% of the solute is transformed purely via surface growth, indicating the growth behavior can be improved. The fraction increases dramatically to ≈90% when R_d is reduced to 0.26 nm s^{-1} and decreases somewhat to 25% when R_d is increased to 2.28 nm s^{-1}. As expected, the transition from predominantly surface-driven growth to mixed (surface

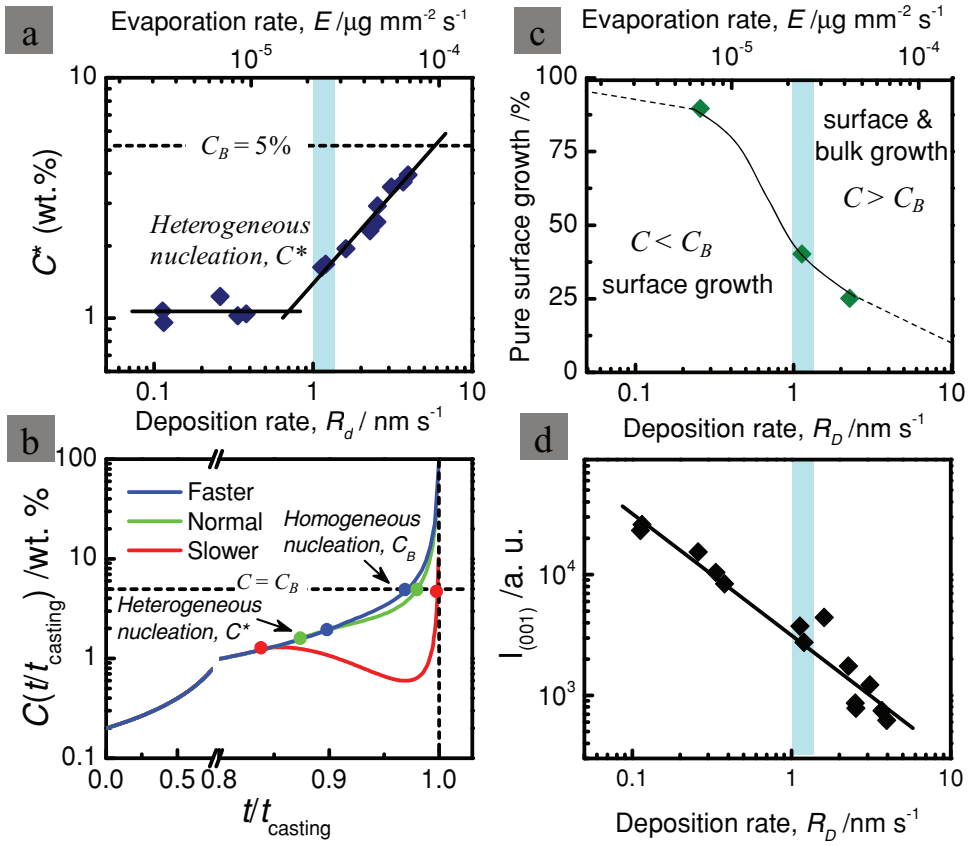

Figure 2. a) The critical concentration for heterogeneous nucleation, C^*, determined from QCM-D experiments. The data reveal a rate-invarient behavior in conditions of slow evaporation and a rate-dependent behavior in ambient and accelerated drying conditions. b) The time-evolution of the concentration of the TIPS-Pn solution, $C(t)$, in relation to the normalized casting time ($t/t_{casting}$) at R_d = 0.26 nm s^{-1}(red), 1.23 nm s^{-1} (green) and 2.28 nm s^{-1} (blue). The onset of nucleation is indicated by the solid circles and the solubility limit of TIPS-Pn in toluene ($C = C_B$) is indicated as a horizontal dashed line. c) The fraction of solute deposited while $C < C_B$. d) The intensity of the (001) Bragg sheet with respect to R_d for films deposited on quartz sensors. The vertical blue bands in (a,c,d) correspond to the ambient evaporation condition, where a total of ten experiments were performed to collect significant statistics. The solubility limit of TIPS-Pn, C_B = 5%, is indicated as a horizontal dashed line.

and bulk) nucleation and growth degrades the lamellar structure, as shown by XRD measurements (see Figure S3, Supporting Information). All samples show purely (001) textured films in XRD measurements with no evidence of any alternate texture or polymorph. The diffraction peak intensities decrease significantly and monotonously with increasing R_d, as this leads to less lamellar crystallization (Figure 2d). Noting that all experiments are performed with the same starting mass of solute, this proves that the ability of the thin film to attain the lamellar texture, which is of great importance to small-molecule OFETs, is significantly hindered by the onset of mixed growth mode. The absence of diffraction peaks other than the lamellar structure in both XRD and GIWAXS suggests that mixed growth leads to loss of long range order, possibly through increased disorder in the deposit formed at the end of the rapid drying experiments.

Cross-polarized optical micrographs (**Figure 3**a,d) and atomic force microscopy (AFM) images (Figure 3b,c and e,f) confirm these observations. At low R_d, flat, ribbon-like domains form, leading to the formation of a thin film with high coverage of the substrate, characterized by large, contiguous and flat platelet-like domains, consistent with predominantly surface-dominated, quasi layer-by-layer formation of the (001)-terminated lamellar structure of TIPS-Pn. The high magnification AFM microscopy images (Figures 3c,f) of the surface of these platelets reveals molecularly flat (001)-facets of TIPS-Pn crystals decorated with small, ≈1–2 monolayer deep pits. Increasing R_d to 2.28 nm s^{-1}, results in the formation of a film with lower surface coverage, characterized by fewer and isolated platelets decorated with much taller (lighter color), three-dimensional (3D) mound-like features. These mounds are round and appear to be dome shaped with a height-to-width aspect ratio of ≈0.1, consistent with formation of highly disordered TIPS-Pn islands formed by rapid homogeneous nucleation and precipitation in the final stages of drying.

This growth model is illustrated in **Figure 4**, where molecules incorporated *via* surface growth regime ($C < C_B$) are shown in grey and molecules incorporated or deposited when $C > C_B$ are shown in red. In conditions of ambient evaporation of the solution (Figure 4a), nearly 60% of molecules are deposited in the

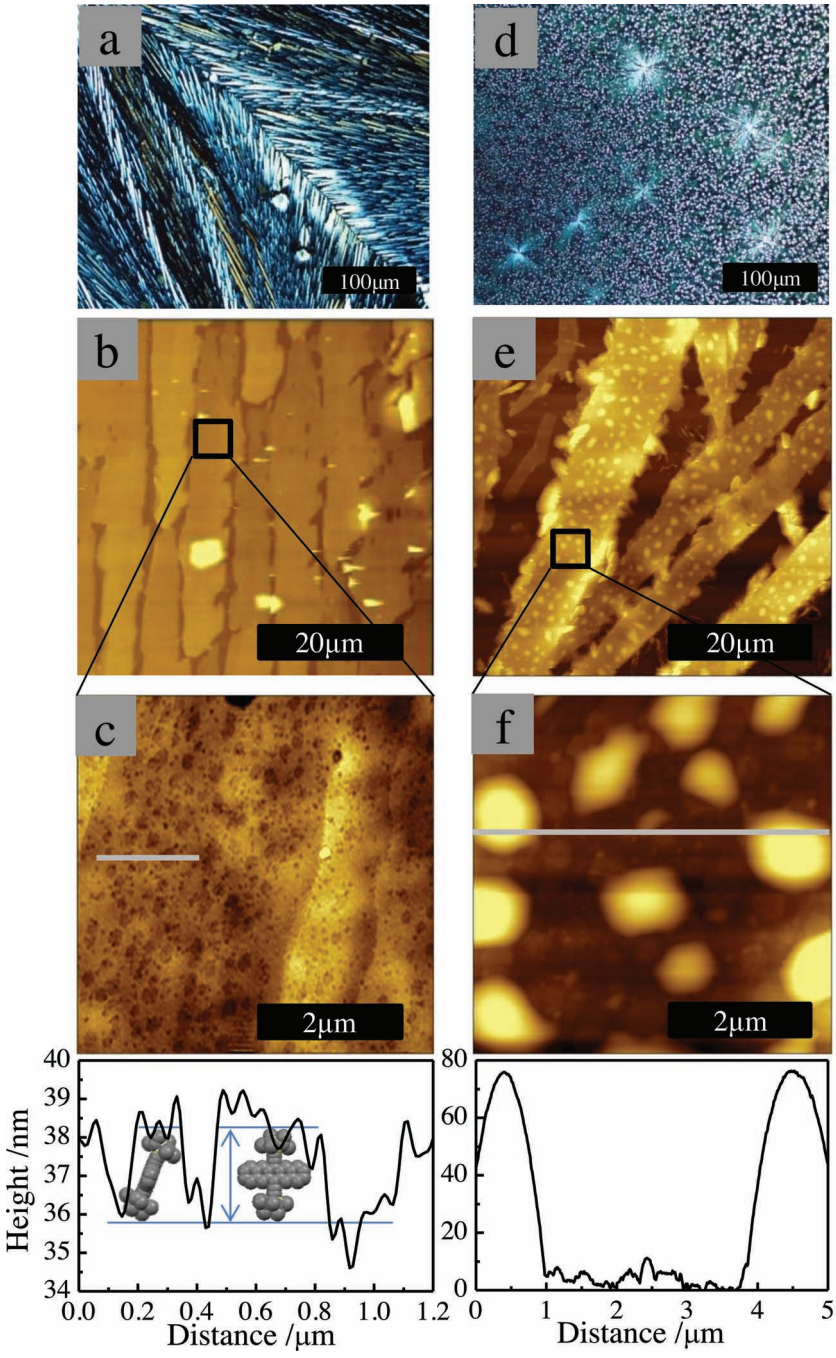

Figure 3. a,d) Cross-polarized optical micrographs and AFM images in b,e) low and c,f) high magnification with line profiles of the surface topography of TIPS-Pn thin films deposited at $R_d = 0.26$ nm s^{-1} (a–c) and $R_d = 2.28$ nm s^{-1} (d–f).

mixed regime. By slowing down the process further (Figure 4b), 90% of molecules are surface incorporated, leading to a highly lamellar textured film. Conversely, nearly 75% of molecules are deposited in the mixed regime when the evaporation is hastened (Figure 4c).With the ability to control the relative growth of the lamellar structure via tuning of the nucleation behavior, we have fabricated several top-contact OFETs using a broad range of drying conditions of the solution. All experiments were monitored using a digital balance, allowing us to relate the resultant device characteristics to R_d (**Figure 5**, and Figure S4,S5 in the Supporting Information). Hole mobility increases fourfold by reducing R_d by an order of magnitude from 1 nm s^{-1} to 0.1 nm s^{-1}, thus increasing the fraction of lamellar growth from 40% to above 90%. Meanwhile, faster drying conditions with R_d up to 6 nm s^{-1} lead to a catastrophic drop in carrier mobility, suggesting that the lamellar structure and film continuity near the semiconductor-dielectric interface are severely compromised by earlier onset of the mixed growth regime.[31]

The insight into the dependence of heterogeneous *versus* homogeneous nucleation upon the kinetics of drying can help explain the observation of generally lower carrier transport in case of spin-cast films *versus* drop-cast films of TIPS-Pn.[6] The slow rate of drying in drop-casting, typically hundreds of seconds when using toluene, allows surface growth to proceed at the expense of bulk growth, whereas much faster rates of drying in case of spin-casting in the order of seconds can be expected to blur the line between the onsets of heterogeneous and homogeneous nucleation. Spin-casting should therefore result in a predominantly mixed growth mode with significant disorder. Nevertheless, the fast drying of the solution being one to two orders of magnitude faster in case of spin-casting has the slight advantage of producing continuous films since the solute solidifies on time scales much shorter than dewetting.[32,33] While continuous coverage of the substrate can mitigate some of the negative effects of forming a partially disordered film by spin-casting, transport is far better when thin film continuity and lamellar structure at the semiconductor-dielectric interface are combined by careful control of the processing kinetics, as demonstrated in this article.

3. Conclusion

In conclusion, we have investigated the growth of TIPS-Pn thin films during drop-casting, using several in situ growth-monitoring techniques complemented by ex situ structural and morphological investigations, as well as field effect mobility measurements. The combination of QCM-D and GIWAXS with simple weight monitoring measurements provides unprecedented insights into the heterogeneous and homogeneous nucleation and growth behaviors of polycrystalline thin films under a broad range of drying conditions. The QCM-D detects the timeline and kinetics of key processes associated with drop-casting and accurately determines the phase status (solid versus

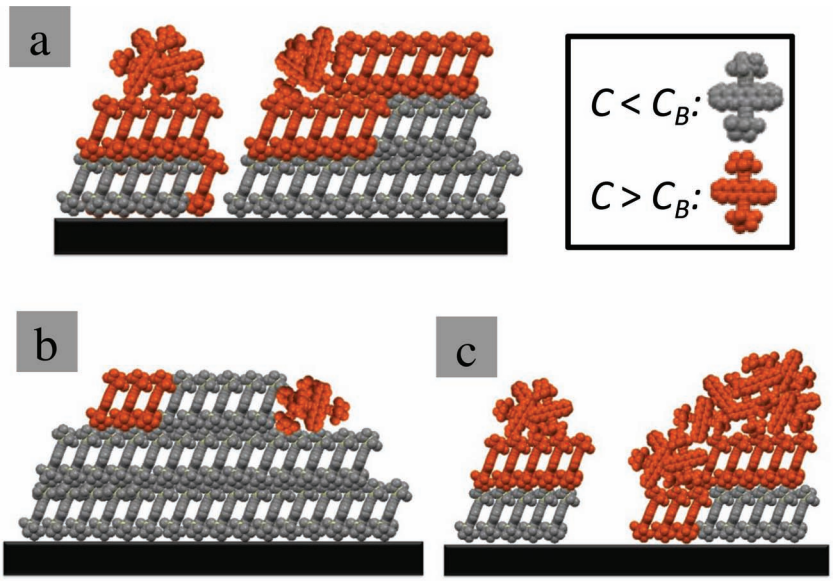

Figure 4. Schematic representations of TIPS-Pn films drop-cast under conditions of a) ambient, b) slow and c) fast drying. The grey and orange molecules refer to parts of the thin film formed via pure heterogeneous nucleation and surface incorporation ($C < C_B$) and by a mixture of surface and bulk growth modes ($C > C_B$), respectively.

liquid) of the films. Combining this information with thin film crystallization kinetics and knowledge of the mean solution concentration allows us to obtain quantitative insights into the time-evolution of a solution concentration during the drying process. Thin film growth was found to be initiated by heterogeneous nucleation occurring at a critical concentration of $C^* \approx 1$ wt% of TIPS-Pn in toluene near the solid-liquid interface. Correct estimation of C^* requires growth experiments to be performed in the heterogeneous nucleation and surface growth regime,

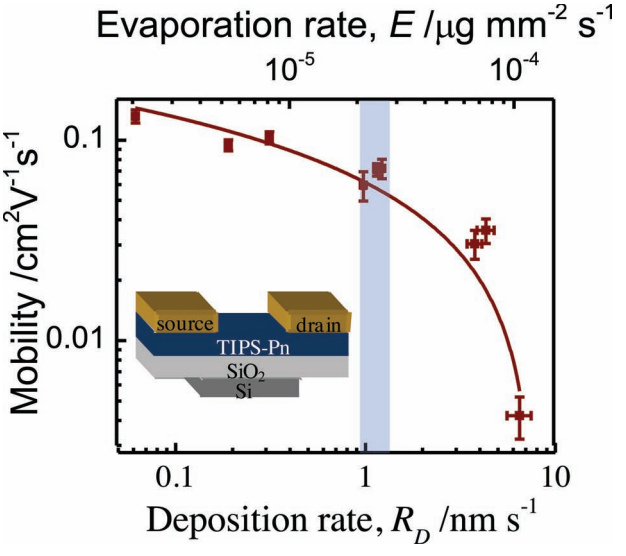

Figure 5. The hole mobility of TIPS-Pn OFETs prepared on bare SiO_2 with respect to R_d and the evaporation rate, E. The vertical band corresponds to the ambient drying condition.

which, in cases of high vapor pressure solvents, is done by reducing the rate of drying, preferably while maintaining a constant process temperature, such as made possible by using an environmental chamber. Tuning the kinetics of drying allows us to determine the growth behavior of the film. Investigation of the structure and morphology of TIPS-Pn using XRD and AFM, respectively, reveals that the kinetics of film formation strongly influences crystallinity and growth behaviors, as indicated by the steadily decreasing lamellar diffraction intensity with increasing deposition rate, as well as by the formation of disordered mounds on the surface of TIPS-Pn crystallites. Slow evaporation insures orderly growth of the lamellar structure by nearly all of the available solute and thus results in high carrier mobility, whereas fast evaporation of the solvent causes the film growth mode to change prematurely from lamellar to disordered and leads to catastrophic reduction of carrier mobility in the conditions investigated herein.

4. Experimental Section

The drop-casting experiments were performed on SiO_2 coated quartz crystal sensors and thermally oxidized Si(001) wafers. The AT-cut quartz crystal sensors (5 MHz resonance frequency, Q-sense, BiolinScientific), with an active area of 12 mm^2, were coated with a 10 nm Au layer and terminated with a 100 nm thick SiO_2 layer, exhibiting a root mean squared surface roughness of ≈1 nm, as determined by AFM. The Si(001) and quartz crystal sensors were cleaned in an ultrasonic bath of acetone, isopropanol and ethanol in 10 min sequences. UV/ozone treatment was performed for 10 min both before and after the cleaning procedure. Solutions were prepared by stirring TIPS-Pn (supplied by JEA) in toluene (Sigma Aldrich) with a concentration of 0.2 wt%.

QCM-D measurements were performed at room temperature in a custom-built environmental chamber utilizing the Open Module accessory of the E4 instrument (Q-sense, BiolinScientific). A 4 µL solution was dropped on the surface of the quartz crystal sensor and the solution drying speed was controlled by sealing the chamber and regulating the N_2 gas flow rate through the enclosed chamber. The ambient condition experiments were performed by drying the solution by removing the top lid of the chamber.

In situ GIWAXS measurements were collected at D-line in the Cornell High Energy Synchrotron Source (CHESS; Cornell University). A wide bandpass (1.47%) double-bounce multilayer monochromator supplied an intense beam with a wavelength of 1.23 Å. A wafer was placed inside the enclosed chamber and N_2 flow rate conditions were set to identical conditions as QCM-D experiments performed in the lab. The incidence angle was set to 0.15° with respect to the substrate plane and a CCD detector (Medoptics) with a pixel size of 46.9 µm was placed at a distance of 92.1 mm from the sample. A 1.5 mm-wide tantalum rod was used to block the intense scattering at low angles of incidence. The recording speed of patterns reached 6 s per image with an exposure time of 1 s.

All samples were subjected to ex situ X-ray diffraction (XRD) measurements in the $\theta/2\theta$ mode with 2θ ranging from 4° to 20° on a Bruker X-pert diffractometer. The beam slits were set to 1 mm × 1 mm. AFM images were obtained in the tapping mode using an Agilent 5400 instrument. The mass change during the drop-casting process was

monitored as a function of time on a balance (Mettler Toledo model AB135-S) with a detection limit of 0.1 mg.

A highly doped n-type silicon wafer (100) with thermally evaporated 300 nm SiO_2 was used for bottom gate, top contact OFET fabrication. Initially the substrates were cleaned by rinsing with acetone, isopropanol, ethanol, and DI water followed by Standard Clean 1 (RCA) ammonium hydroxide (30% NH_4OH), hydrogen peroxide (30% H_2O_2) and DI water (with 1:1:5 ratio) for 30 minutes at 70 °C. All substrates were blown dry with N_2 and heated at 100 °C for 20 min before transferring to the nitrogen glove box. 4 µL solutions of TIPS-Pn in toluene (0.2 wt.%) were drop-cast onto Si substrates placed on a balance inside the glove box with N_2 gas circulated at different flow rates to vary and monitor the evaporation and deposition rates. Gold source and drain electrodes were deposited by evaporation through a shadow mask with a channel width (W) of 500 µm and length (L) of 50 µm. All electrical measurements were performed with a Keithley 4200 Semiconductor Characterization System under N_2 atmosphere inside the glove box.

Supporting Information

Supporting Information is available from the Wiley Online Library or from the author.

Acknowledgements

The authors are grateful to Mr. Mohammed Balamesh for his important contributions to the operational readiness of the Organic Electronics and Photovoltaics Laboratory at King Abdullah University of Science and Technology, where most of this work was performed. Part of this work was supported by KAUST's Office of Competitive Research Funds under award number FIC/2010/04. The authors acknowledge use of the D1 beam line at the Cornell High Energy Synchrotron Source supported by the National Science Foundation (NSF DMR-0225180) and NIH-NIGMS.

Received: May 9, 2012
Revised: July 24, 2012
Published online: September 4, 2012

[1] S. R. Forrest, *Nature* **2004**, *428*, 911.
[2] V. C. Sundar, J. Zaumseil, V. Podzorov, E. Menard, R. L. Willett, T. Someya, M. E. Gershenson, J. A. Rogers, *Science* **2004**, *303*, 1644.
[3] L. Wang, M.-H. Yoon, G. Lu, Y. Yang, A. Facchetti, T. J. Marks, *Nat. Mater.* **2007**, *6*, 317.
[4] R. Hamilton, J. Smith, S. Ogier, M. Heeney, J. E. Anthony, I. McCulloch, J. Veres, D. D. C. Bradley, T. D. Anthopoulos, *Adv. Mater.* **2009**, *21*, 1166.
[5] S. K. Park, D. A. Mourey, J. I. Han, J. E. Anthony, T. N. Jackson, *Org. Electron.* **2009**, *10*, 486.
[6] S. K. Park, T. N. Jackson, J. E. Anthony, D. A. Mourey, *Appl. Phys. Lett.* **2007**, 91.
[7] J. Smith, W. Zhang, R. Sougrat, K. Zhao, R. Li, D. Cha, A. Amassian, M. Heeney, I. McCulloch, T. D. Anthopoulos, *Adv. Mater.* **2012**, *24*, 2441
[8] T. Hasegawa, H. Minemawari, T. Yamada, H. Matsui, J. Tsutsumi, S. Haas, R. Chiba, R. Kumai, *Nature* **2011**, *475*, 364.
[9] S. S. Lee, C. S. Kim, E. D. Gomez, B. Purushothaman, M. F. Toney, C. Wang, A. Hexemer, J. E. Anthony, Y.-L. Loo, *Adv. Mater.* **2009**, *21*, 3605.
[10] G. Giri, E. Verploegen, S. C. B. Mannsfeld, S. Atahan-Evrenk, D. H. Kim, S. Y. Lee, H. A. Becerril, A. Aspuru-Guzik, M. F. Toney, Z. Bao, *Nature* **2011**, *480*, 504.
[11] J. Rivnay, L. H. Jimison, J. E. Northrup, M. F. Toney, R. Noriega, S. F. Lu, T. J. Marks, A. Facchetti, A. Salleo, *Nat. Mater.* **2009**, *8*, 952.
[12] R. Li, J. W. Ward, D.-M. Smilgies, M. M. Payne, J. E. Anthony, O. D. Jurchescu, A. Amassian, *Adv. Mater.* **2012**, DOI: 10.1002/adma.201201856.
[13] B. Schmidt-Hansberg, M. F. G. Klein, K. Peters, F. Buss, J. Pfeifer, S. Walheim, A. Colsmann, U. Lemmer, P. Scharfer, W. Schabel, *J. Appl. Phys.* **2009**, *106*, 124501.
[14] C. D. Dimitrakopoulos, P. R. L. Malenfant, *Adv. Mater.* **2002**, *14*, 99.
[15] J. A. Lim, H. S. Lee, W. H. Lee, K. Cho, *Adv. Funct. Mater.* **2009**, *19*, 1515.
[16] S. Hong, A. Amassian, A. R. Woll, S. Bhargava, J. D. Ferguson, G. G. Malliaras, J. D. Brock, J. R. Engstrom, *Appl. Phys. Lett.* **2008**, *92*, 253304.
[17] D. Kafer, L. Ruppel, G. Witte, *Phys. Rev. B* **2007**, 75.
[18] S. Kowarik, A. Gerlach, F. Schreiber, *J. Phys.: Condens. Matter* **2008**, 20.
[19] R. Ruiz, B. Nickel, N. Koch, L. C. Feldman, R. F. Haglund Jr., A. Kahn, F. Family, G. Scoles, *Phys. Rev. Lett.* **2003**, *91*, 136102.
[20] L. N. Arnaudov, *J. Chem. Phys.* **2006**, *124*, 084701.
[21] L. Yang, P. Alexandridis, D. C. Steytler, M. J. Kositza, J. F. Holzwarth, *Langmuir* **2000**, *16*, 8555.
[22] J. Smith, R. Hamilton, I. McCulloch, N. Stingelin-Stutzmann, M. Heeney, D. D. C. Bradley, T. D. Anthopoulos, *J. Mater. Chem.* **2010**, *20*, 2562.
[23] D. M. Smilgies, D. R. Blasini, *J. Appl. Crystallogr.* **2007**, *40*, 716.
[24] K. A. Marx, *Biomacromolecules* **2003**, *4*, 1099.
[25] M. Rodahl, B. Kasemo, *Sens. Actuators, B* **1996**, *37*, 111.
[26] V. M. Mecea, *Anal. Lett.* **2005**, *38*, 753.
[27] G. Sauerbrey, *Zeit. Phys. A: Nucl.* **1959**, *155*, 206.
[28] M. Avrami, *J. Chem. Phys.* **1939**, *7*, 1103.
[29] B. T. Holland, C. F. Blanford, T. Do, A. Stein, *Chem. Mater.* **1999**, *11*, 795.
[30] R. S. Ho Lam, M. A. Rogers, *Cryst. Eng. Comm.* **2011**, *13*, 866.
[31] K. C. Dickey, J. E. Anthony, Y. L. Loo, *Adv. Mater.* **2006**, *18*, 1721.
[32] D. B. Mitzi, L. L. Kosbar, C. E. Murray, M. Copel, A. Afzali, *Nature* **2004**, *428*, 299.
[33] A. Amassian, V. A. Pozdin, T. V. Desai, S. Hong, A. R. Woll, J. D. Ferguson, J. D. Brock, G. G. Malliaras, J. R. Engstrom, *J. Mater. Chem.* **2009**, *19*, 5580.